

# A Comprehensive Mechanism of Fibrin Network Formation Involving Early Branching and Delayed Single- to Double-Strand Transition from Coupled Time-Resolved X-ray/Light-Scattering Detection

Mattia Rocco,<sup>\*,†,○</sup> Matteo Molteni,<sup>‡,○</sup> Marco Ponassi,<sup>†</sup> Guido Giachi,<sup>§</sup> Marco Frediani,<sup>§</sup> Alexandros Koutsioubas,<sup>⊥,∇</sup> Aldo Profumo,<sup>†</sup> Didier Trevarin,<sup>⊥</sup> Barbara Cardinali,<sup>||,¶</sup> Patrice Vachette,<sup>#,⊗,○</sup> Fabio Ferri,<sup>‡,○</sup> and Javier Pérez<sup>⊥,○</sup>

<sup>†</sup>Biopolimeri e Proteomica, IRCCS AOU San Martino-IST, I-16132 Genova, Italy

<sup>‡</sup>Dipartimento di Scienza e Alta Tecnologia and *To.Sca.Lab*, Università dell'Insubria, I-22100 Como, Italy

<sup>§</sup>Dipartimento di Chimica "Ugo Schiff", Università di Firenze, I-50019 Sesto Fiorentino, Italy

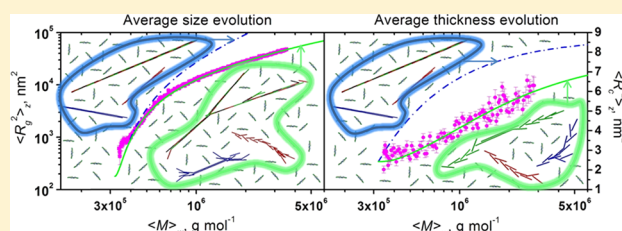
<sup>⊥</sup>SWING Beamline, Synchrotron SOLEIL, L'Orme des Merisiers, Saint-Aubin, F-91192 Gif-sur-Yvette, France

<sup>||</sup>Department of Pathology and Laboratory Medicine, University of North Carolina at Chapel Hill, Chapel Hill, North Carolina 27599-7525, United States

<sup>#</sup>IBBMC, UMR8619, Université Paris-Sud, and <sup>⊗</sup>CNRS, F-91405 Orsay, France

## Supporting Information

**ABSTRACT:** The formation of a fibrin network following fibrinogen enzymatic activation is the central event in blood coagulation and has important biomedical and biotechnological implications. A non-covalent polymerization reaction between macromolecular monomers, it consists basically of two complementary processes: elongation/branching generates an interconnected 3D scaffold of relatively thin fibrils, and cooperative lateral aggregation thickens them more than 10-fold. We have studied the early stages up to the gel point by fast fibrinogen:enzyme mixing experiments using simultaneous small-angle X-ray scattering and wide-angle, multi-angle light scattering detection. The coupled evolutions of the average molecular weight, size, and cross section of the solutes during the fibrils growth phase were thus recovered. They reveal that extended structures, thinner than those predicted by the classic half-staggered, double-stranded mechanism, must quickly form. Following extensive modeling, an initial phase is proposed in which single-bonded "Y-ladder" polymers rapidly elongate before undergoing a delayed transition to the double-stranded fibrils. Consistent with the data, this alternative mechanism can intrinsically generate frequent, random branching points in each growing fibril. The model predicts that, as a consequence, some branches in these expanding "lumps" eventually interconnect, forming the pervasive 3D network. While still growing, other branches will then undergo a  $\text{Ca}^{2+}$ /length-dependent cooperative collapse on the resulting network scaffolding filaments, explaining their sudden thickening, low final density, and basic mechanical properties.



## INTRODUCTION

The formation of a fibrin network is the central event in vertebrates' blood coagulation.<sup>1,2</sup> It is also involved in several pathologies, such as thrombosis and cancer metastasis (e.g., refs 2, 3), and is of great biomedical/biotechnological relevance (e.g., refs 4, 5). Physiologically, it represents the end of the coagulation cascade when thrombin activates the inactive precursor fibrinogen (FG).<sup>2,6,7</sup> FG is a centrosymmetric, high-molecular-weight ( $\sim 338\,000\text{ g mol}^{-1}$ ), elongated macromolecule ( $L \approx 46\text{ nm}$ ,  $d \approx 3\text{--}5\text{ nm}$ ) composed of two pairs each of three different chains,  $A\alpha$ ,  $B\beta$ , and  $\gamma$  ( $A\alpha_2B\beta_2\gamma_2$ ).<sup>6,7</sup> All six N-terminals are located in a central globular domain ("E" region), connected by two triple  $A\alpha B\beta\gamma$  coiled-coil segments to two outer distal domains ("D" regions), each formed by the  $B\beta$  and  $\gamma$  chains' individually folded C-terminal domains; the

location of the  $A\alpha$  chains'  $>400$  C-terminal residues (" $\alpha$ C" regions) is still mostly undetermined<sup>6–10</sup> (see Figure 1A,B). Thrombin initially cleaves a pair of small peptides (fibrinopeptides A, FpA) from the N-terminal ends of the  $A\alpha$  chains in the central FG E region. The new  $\alpha$  chains' Gly-Pro-Arg N-terminals ("A" knobs) can fit into pockets (" $a$ " holes) constitutively available in the D regions'  $\gamma$  chain domain<sup>2,6–10</sup> of another FG unit (Figure 1B). In the currently accepted mechanism, a half-staggered dimer is formed by a pair of reciprocal  $A$ - $a$  knob-hole center-to-end non-covalent binding events. By further addition of monomers and oligomers, a rod-like or worm-like double-stranded (RLDS/WLDS) fibril is then

Received: January 10, 2014

Published: March 21, 2014

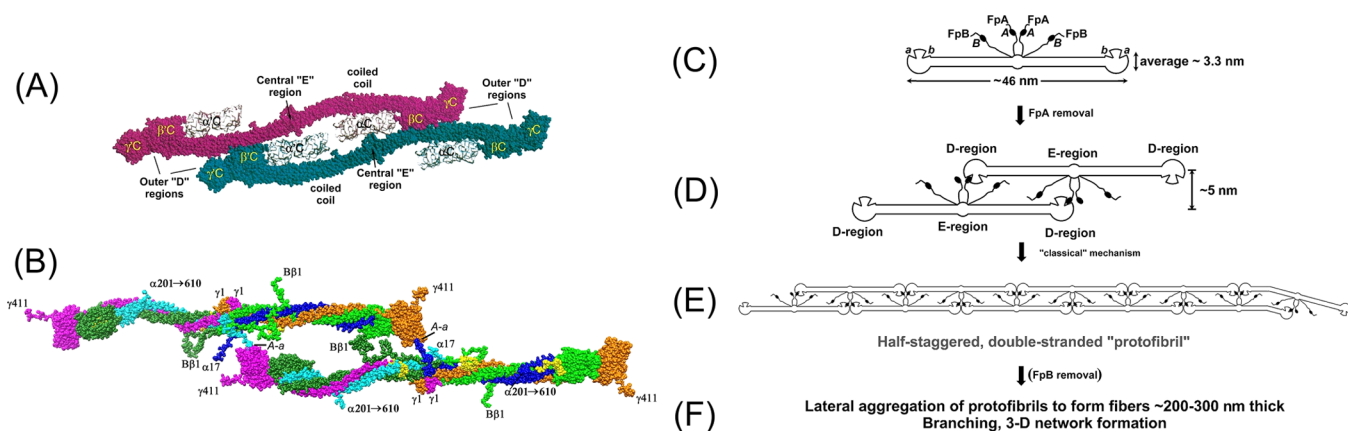


**Figure 1.** Fibrinogen structure and the “classic” fibrin polymerization mechanism. (A) Crystallographic dimer of chicken FG (adapted from ref 9), with indicated the central “E” and outer “D” regions and the coiled-coil connectors. The  $B\beta$  and  $\gamma$  chains’ C-terminal domains ( $\beta C$  and  $\gamma C$ , respectively) are also marked. The white “blobs” marked  $\alpha C$  are the electron densities of unresolved  $A\alpha$  chains’ C-terminal regions. (B) A model of Ancrod-activated FG in the classic half-staggered dimer configuration (only the FpA are removed; the  $\alpha C$  domains are not resolved). Color coding: blue and cyan,  $\alpha$  chains; green and forest green,  $B\beta$  chains; orange and magenta,  $\gamma$  chains; yellow, carbohydrates. Main body coordinates taken from the human FG structure.<sup>10</sup> The conformation of the  $\alpha 17$ –27,  $B\beta 1$ –54, and  $\gamma 398$ –411 segments is only putative. Indicated are the locations of relevant N- and C-terminal ends of the chains and the engagement of the two A-a knob–hole interactions. (C–F) Schematic representation of FG (C) and of the classic mechanism of fibrin formation, starting with a half-staggered dimer (D), growing into a rod-like (or worm-like) double-stranded protofibril (E), and the later events favored by FpB removal (F).

built (Figure 1C–E). Later on, thrombin cuts a second pair of peptides (fibrinopeptides B, FpB) from the  $B\beta$  chains’ N-terminals. The new Gly-His-Arg N-terminals (“B” knobs) can fit into constitutively available pockets (“b” holes) in the D regions’ ( $B\beta$  chain domains). This produces a subtle conformational change favoring the lateral aggregation of tens of fibrils into 200–300 nm thick fibers<sup>11</sup> (Figure 1F). Importantly, this  $Ca^{2+}$ -sensitive second step happens in dramatic fashion near the gel point, as originally evidenced by turbidity data showing a lag-time phase with no apparent changes followed by a sudden rise of the signal.<sup>2,6,7</sup>

Notwithstanding hundreds of fibrin polymerization studies (see ref 7 and references therein), the details of the network formation have remained elusive. Electron microscopy (EM) has proved the existence of the half-staggered, double-stranded (proto)fibrils<sup>12,13</sup> but cannot perform truly time-resolved experiments, and short-lived or fragile structures might be missed. New insights have been recently provided by advanced light microscopies,<sup>14,15</sup> but the resolution is too low to extract truly structural details. Alternatively, a wide variety of time-resolved light-scattering (LS) techniques have been employed to study fibrin polymerization, yielding, however, only ensemble-averaged data (e.g., refs 16–24). In the early 2000s, wide-angle multi-angle light-scattering (WA-MALS) and low-angle elastic light-scattering (LAELS) with rapid mixing were used to study both the early and later phases.<sup>21–24</sup> For the initial stages, the coupled evolution of the z-average square radius of gyration  $\langle R_g^2 \rangle_z$  and of the weight-average molecular weight  $\langle M \rangle_w$  could be extracted from WA-MALS data.<sup>21,22</sup> Surprisingly, these data were incompatible with the classic half-staggered RLDS mechanism when simulated using modified Flory bifunctional polycondensation distributions,<sup>21,22,25</sup> suggesting the formation of more elongated, thinner structures later coalescing into the classic RLDS/WLDS fibrils.<sup>21,22</sup> The data also implied that the ratio of release  $Q$  between the two FpA from any individual FG molecule was  $\gg 1$ , meaning a faster cleavage of the second FpA and thus significantly skewing the distribution toward longer polymers.<sup>21,22</sup> However, a crucial

parameter to prove this alternative mechanism, the coupled evolution of the fibrils’ thickness (in the form of the mass/length ratio  $\langle M/L \rangle_{w/z}$ ), could not be obtained from WA-MALS data until later in the reaction because of fundamental instrumental limitations.<sup>21,22,26</sup>

Solution small-angle X-ray scattering (SAXS) can instead provide the solutes’ z-average cross-sectional square radius of gyration  $\langle R_c^2 \rangle_z$  in a time-resolved manner.<sup>27</sup> However, it cannot simultaneously measure the  $\langle R_g^2 \rangle_z$  and  $\langle M \rangle_w$  beyond those of small oligomers, since their rapid growth quickly leads to values outside the setup’s accessible length scales. Thus, in order to determine simultaneously all three parameters, we have coupled a commercial flow-cell WA-MALS with the SWING beamline SAXS flow capillary at the Synchrotron SOLEIL (Gif-sur-Yvette, France), achieving fast mixing with a modified four-syringe stopped-flow device. The snake venom enzyme Ancrod, which removes only the FpA,<sup>28</sup> was used instead of thrombin to avoid even limited FpB cleavage. Experiments were performed in a buffer approaching physiological conditions, without and with added  $Ca^{2+}$ , and also in the presence of the A knob competing peptide Gly-Pro-Arg-Pro amide (GPRP-NH<sub>2</sub>). We present here the results of our studies, which have led us to propose an alternative and comprehensive fibrin polymerization scheme. We would also like to point out that the novel SAXS/MALS combination developed in the present study could be profitably employed to study the structural dynamics of other processes involving the elongation and thickening of fibrous-like structures (e.g., collagen,  $\beta$ -amyloid).

## ■ MATERIALS AND METHODS

**Sample Preparation.** A full description is available in the Supporting Information. The main buffer used was tris-(hydroxymethyl)aminomethane 50 mM, NaCl 104 mM, aprotinin 10 kIU/mL, pH 7.4 (TBS).

**Stopped-Flow/WA-MALS/SAXS Setup.** The overall goal of the setup was to have a remotely controlled system that could (i) perform repeated reactions with both WA-MALS and SAXS simultaneous detection without the need to enter the X-ray equipment enclosure; (ii) avoid cross-contamination between the reservoirs containing the

Table 1. Starting Parameters Established by SAXS and WA-MALS QELS<sup>a</sup>

sample	SAXS			WA-MALS QELS		
	$[\langle R_g^2 \rangle_z]^{1/2}$ (nm)	$\langle M \rangle_w$ ( $\times 10^{-5}$ g mol <sup>-1</sup> )	$[\langle R_c^2 \rangle_z]^{1/2}$ (nm)	$[\langle R_g^2 \rangle_z]^{1/2}$ (nm)	$\langle M \rangle_w$ ( $\times 10^{-5}$ g mol <sup>-1</sup> )	$\langle R_s \rangle_z$ (nm)
FG	14.4 $\pm$ 0.2	3.30 $\pm$ 0.003	1.8 $\pm$ 0.1	14.6 $\pm$ 0.02	3.37 $\pm$ 0.002	10.3 $\pm$ 0.05
FG + GPRP-NH <sub>2</sub> <sup>b</sup>	14.6 $\pm$ 0.2	3.34 $\pm$ 0.003	1.5 $\pm$ 0.1	14.4 $\pm$ 0.01	3.40 $\pm$ 0.002	10.4 $\pm$ 0.02
FG + Ca <sup>2+</sup> + GPRP-NH <sub>2</sub> <sup>b</sup>	14.1 $\pm$ 0.2	3.31 $\pm$ 0.002	1.7 $\pm$ 0.1	14.7 $\pm$ 0.01	3.36 $\pm$ 0.002	10.5 $\pm$ 0.02

<sup>a</sup>Reported errors are the SD of the fits, performed after data averaging. WA-MALS detectors were normalized with the SAXS-derived FG  $[\langle R_g^2 \rangle_z]^{1/2}$ .

<sup>b</sup>GPRP-NH<sub>2</sub>:FG molar ratio 500:1.

reactants during the relatively long reaction times (up to 10 min or more); (iii) provide clean, dust-less, undisturbed solutions for WA-MALS data acquisition; and (iv) avoid continuous exposure of the same sample volume to the intense X-ray beam for SAXS data acquisition. A diagram of the final setup is shown in Figure S1, and its implementation and operation are described in detail in the Supporting Information (“Stopped-flow/WA-MALS/SAXS set-up”).

The WA-MALS used (DAWN HELEOS II, Wyatt Technology Corp., Santa Barbara, CA, USA) has 18 photodiodes placed around a fused silica glass cylindrical cell (refractive index  $n = 1.51876$ ), with a small (1.25 mm diameter) horizontal flow-through channel, held by two metal blocks with perpendicular high-performance liquid chromatography (HPLC)-type connectors (cell holdup volume  $\sim 70$   $\mu$ L, scattering volume  $\sim 0.07$   $\mu$ L). The cell was kept at  $20.0 \pm 0.1$  °C by its internal Peltier device. Two polished windows allow illuminating the sample along the cell borehole (120 mW solid-state GaAs linearly polarized laser,  $\lambda = 661$  nm). At these  $\lambda$  and  $T$ ,  $n = 1.3332$  for TBS,<sup>29</sup> making 17 scattering angles available, from 13.5° to 157.5°. Actually, 16 angles are used, because a photodiode placed at  $\sim 100^\circ$  is replaced with a fiber-optic connection for dynamic light scattering measurements (also known as quasi-elastic light scattering (QELS), Wyatt Technology Corp.).

The SWING beamline technical specifications and the Bio-SAXS setup utilized in this study are described elsewhere.<sup>30,31</sup> Briefly, a low-noise  $160 \times 160$  mm<sup>2</sup> charge-coupled device (CCD) detector (Aviex, Dexela, UK) is positioned on a motorized stage within a large vacuum chamber, thus allowing for an easy change of the sample-to-detector distance. The SAXS cell consists of a flow-through, thermalized, thin-walled 1.5 mm diameter quartz capillary, positioned within the vacuum chamber and connected to the outside through a lateral flange. Importantly, two optical fibers placed before the X-ray beam allow recording UV–vis spectra through the quartz capillary using a miniature CCD array spectrophotometer (USB2000, Ocean Optics, Dunedin, FL, USA), providing the protein concentration in the scattering cells. For the non-polymerizing FG runs, the SAXS detector distance was set to 4 m to access a small momentum transfer  $q$  useful range ( $0.0032 \text{ \AA}^{-1} < q < 0.18 \text{ \AA}^{-1}$ ;  $q = 4\pi \sin(\theta/2)/\lambda$ , with  $\theta$  the scattering angle and  $\lambda = 1.033 \text{ \AA}$  the incident radiation wavelength) for best estimation of the initial samples'  $\langle R_g^2 \rangle_z$ . This was important, since the resulting FG  $[\langle R_g^2 \rangle_z]^{1/2}$  in TBS was then used to normalize the WA-MALS detectors (see Supporting Information, “WA-MALS data analysis”). For the FG polymerization runs, a SAXS detector distance of  $\sim 2$  m ( $0.00568 \text{ \AA}^{-1} < q < 0.5 \text{ \AA}^{-1}$ ) was then used.

**WA-MALS and SAXS Data Analysis.** A detailed description of all the procedures used in analyzing the WA-MALS and SAXS data can be found in the Supporting Information (“WA-MALS data analysis”, “SAXS data analysis”, and Figures S3–S7).

**Modeling.** Basic modeling was done as already reported in detail.<sup>21,22</sup> FG was modeled as a cylinder with length  $L = 46$  nm and hydrated diameter  $d_h = 4.4$  nm, based on the  $\langle R_g^2 \rangle_z$  and  $\langle R_c^2 \rangle_z$  values from HPLC-SAXS.<sup>32</sup> As we previously suggested,<sup>32</sup> we interpret the experimental  $\langle R_c^2 \rangle_z$  data as deriving from the weight-average square cross-sectional radius<sup>33</sup> along the principal axis of the FG main body and of the  $\alpha$ C domains. To account for an average molecular mass of  $\sim 320\,000$  g mol<sup>-1</sup> (due to the weak polydispersity of our FG samples<sup>34</sup>), and considering a theoretical hydration of 0.42 g H<sub>2</sub>O/g FG (calculated by PROMOL35), an anhydrous diameter  $d_a = 4.1$  nm and a density  $\rho_a = 0.875$  g cm<sup>-3</sup> were employed. The latter is considerably lower than the 1.393 g cm<sup>-3</sup> computed from the FG

composition, likely reflecting the mostly disordered  $\alpha$ C regions being positioned away from the FG main body. The monomer radius of gyration and cross-sectional radius of gyration, computed via the formulas  $R_g^2 = (L^2/12) + (d_a^2/8)$  and  $R_c^2 = d_h^2/8$ , were  $R_g = 13.4$  nm and  $R_c = 1.56$  nm, respectively. Polymers were explicitly simulated as geometric arrangements of cylinders, for which the  $R_g^2$  and  $M$  could easily be computed. As for  $R_c^2$ , it was computed for each polymer as a weight-average between the single- and double-stranded sections.<sup>33</sup> The lateral separation between the strands in the DS polymers was controlled by an overall density value equal to (touching strands) or less than that of the monomer; 0.787 g cm<sup>-3</sup> gave a reasonable distance between centers  $d_{DS} = 5.02$  nm (see Figure 1). A corresponding cross-sectional radius of gyration  $R_{c(DS)} = 2.95$  nm resulted from the parallel axis theorem,  $R_{c(DS)} = R_c^2 + (d_{DS}/2)^2$ . The basic polymer models included rigid RLDS and flexible WLDS types (for the latter, the Kuhn length  $L_{K(DS)}$  could be varied at will). Polymer distributions were generated according to the Flory bifunctional polycondensation statistics as modified by Janmey<sup>25</sup> to account for a different rate of release  $Q$  between the two FpA in a single FG molecule (see ref 21 and references therein). Since  $K_M$  and  $k_{cat}$  for the Ancred–human FG system are not available, the human thrombin–bovine FG values of  $K_M = 9.2 \times 10^{-6}$  M and  $k_{cat} = 7.3 \times 10^{-7}$  mL s<sup>-1</sup> NIH-unit<sup>-1</sup> were used (see ref 21 and references therein). In any case, this does not affect the simulations, since the time factor is removed by plotting the computed  $\langle R_g^2 \rangle_z$  and  $\langle R_c^2 \rangle_z$  vs  $\langle M \rangle_w$ . The  $\langle R_g^2 \rangle_z$ ,  $\langle R_c^2 \rangle_z$ , and  $\langle M \rangle_w$  values at any time point are easily obtained from the synthetic polymer distributions.

The alternative Y-ladder (YL) modeling that we have developed (see Results) also led to an investigation of their SAXS properties (see Supporting Information, “YL models definition and scattering properties” and Figures S6 and S7). For this alternative modeling, it was also necessary to generate a great number of explicit polymer conformations at each polymerization degree, whose parameters were then averaged. This long and somewhat complex procedure is fully described in the Supporting Information (“YL→DS models generation and parameters computation” and Figures S9–S11).

**Contact Conditions Evaluation.** The ratio  $d^*/a^*$  between the number-average diameter  $d^* = (\langle d^3 \rangle_n)^{1/3}$  of spheres representing the FG polymers and their number-average distance  $a^* = (\langle a^3 \rangle_n)^{1/3}$  for all polymers present in our simulations at any particular  $\langle M \rangle_w$  value was evaluated in the following way. First, the average radius  $\langle r^2(i) \rangle_n$  of the equivalent sphere for each type of polymer made of  $i$  monomers was computed from their average  $\langle R_g^2(i) \rangle_n$  as  $\langle r^2(i) \rangle_n = (5/3)\langle R_g^2(i) \rangle_n$ . From the theoretical polymer distribution as a function of the polymerization degree, the volume fraction  $\phi$  occupied by the polymers at any  $\langle M \rangle_w$  value is  $\phi_{(M)_w} = \sum_i (v_i c_{FG} w_i N_A / M_i)$ , where  $v_i$ ,  $w_i$ , and  $M_i$  are the volume ( $v_i = (4/3)\pi(\langle r(i) \rangle_n)^3$  [cm<sup>3</sup>], weight fraction, and molecular weight [g mol<sup>-1</sup>] of the  $i$ th polymer, respectively,  $N_A$  is Avogadro's number, and  $c_{FG}$  is the initial FG concentration [g cm<sup>-3</sup>]. Finally,  $d^*/a^*$  was evaluated from the relation<sup>36</sup>  $(d^*/a^*)_{(M)_w} = (6\phi_{(M)_w}/\pi)^{1/3}$ .

## RESULTS

The novel stopped-flow/WA-MALS/SAXS setup that we have developed has allowed us to perform static and time-resolved simultaneous acquisitions of both WA-MALS and SAXS data. Its implementation and detailed description are reported in the

Supporting Information (“Stopped-flow/WA-MALS/SAXS setup” and Figures S1 and S2). Before the polymerization experiments, FG SAXS and WA-MALS datasets were collected in TBS and TBS + GPRP-NH<sub>2</sub> 1 mM without and with Ca<sup>2+</sup> 1.25 mM, to check the starting values for all parameters. In addition, the Stokes radius  $R_S$  was also measured with the WA-MALS QELS device. As can be seen in Table 1, all FG samples showed nearly identical values for most parameters, as well as a good consistency between SAXS and WA-MALS data. While the  $\langle M \rangle_w$  and  $\langle R_g \rangle_z$  values appear to be in excellent agreement with the expected and literature values for FG (see ref 34), the  $\langle R_g^2 \rangle_z$  and  $\langle R_c^2 \rangle_z$  values, somewhat higher than those derived from FG HPLC-SAXS experiments,<sup>32</sup> likely reflect a slight but negligible tendency toward self-aggregation. We concluded these characterization and calibration measurements with a simple but crucial control in which the FG solution was mixed with buffer in the absence of enzyme and data were recorded exactly as in a polymerization run. No change was observed in the SAXS pattern with time, thus excluding any radiation-induced effect.

A typical WA-MALS FG polymerization experimental dataset is shown in the Supporting Information (Figure S3A,B). The initiation point was taken at the end of the injection (lasting 9 s), and the reaction was stopped by flushing out the solution just before the gel point to avoid clogging the SAXS capillary. The extensive processing that WA-MALS polymerization data require<sup>21,22</sup> is fully described in the Supporting Information (“WA-MALS data analysis” and Figures S3C–F, S4, and S5). A subset of preprocessed SAXS data corresponding to the WA-MALS data of Figure S3A,B is plotted in Figure S7.

Representative resulting datasets for three Ancrod-induced FG polymerization runs in TBS, TBS + Ca<sup>2+</sup> 1.25 mM, and TBS + GPRP-NH<sub>2</sub> 0.02 mM (at slightly different initial FG concentrations  $c_{FG}$ ) are shown in Figure 2, as the time evolution of  $\langle M \rangle_w$ ,  $\langle R_g^2 \rangle_z$ , and  $\langle R_c^2 \rangle_z$ , where the significant differences between the various conditions and the good quality of the data can be appreciated. Note that the error bars reflect only the statistical uncertainties associated with recovering the average  $\langle M \rangle_w$ ,  $\langle R_g^2 \rangle_z$ , and  $\langle R_c^2 \rangle_z$  values from the experimental data. No attempt was made to extract from the data the distributions of the  $M$ ,  $R_g^2$ , and  $R_c^2$  values as a function of time, as this rapidly becomes a highly degenerate inversion problem.

**Coupled Evolution of  $\langle R_g^2 \rangle_z$  and  $\langle R_c^2 \rangle_z$  versus  $\langle M \rangle_w$ .** It has been previously shown<sup>18,19,21,22</sup> that FG polymerization WA-MALS data can be best interpreted by removing the time factor and plotting  $\langle R_g^2 \rangle_z$  and  $\langle M/L \rangle_{w/z}$  vs  $\langle M \rangle_w$ . Similar plots, with  $\langle R_c^2 \rangle_z$  in place of  $\langle M/L \rangle_{w/z}$  are presented in Figure 3 for the three FG polymerization runs of Figure 2. Confirming our previous reports,<sup>21,22</sup> the addition of Ca<sup>2+</sup> ions, while slowing down the process (see Figure 2), does not significantly affect its mechanism, as both the  $\langle R_g^2 \rangle_z$  vs  $\langle M \rangle_w$  and  $\langle R_c^2 \rangle_z$  vs  $\langle M \rangle_w$  plots (Figure 3A,B, green symbols) follow the same course as the Ca<sup>2+</sup>-less data. Importantly, when the A knob competing inhibitor GPRP-NH<sub>2</sub> is added in a 500:1 molar ratio to FG, it completely impedes any polymer formation, as observed by both WA-MALS and SAXS (not shown), ruling out a previously hypothesized end-to-end/single-strand to half-staggered/DS model.<sup>21,22</sup> However, at rate-limiting GPRP-NH<sub>2</sub> amounts (GPRP-NH<sub>2</sub>:FG 10:1), a difference arises between the  $\langle R_g^2 \rangle_z$  vs  $\langle M \rangle_w$  and  $\langle R_c^2 \rangle_z$  vs  $\langle M \rangle_w$  plots: while the former (Figure 3A, blue squares) still nicely superimposes with the other datasets, the latter (Figure 3B, blue circles)

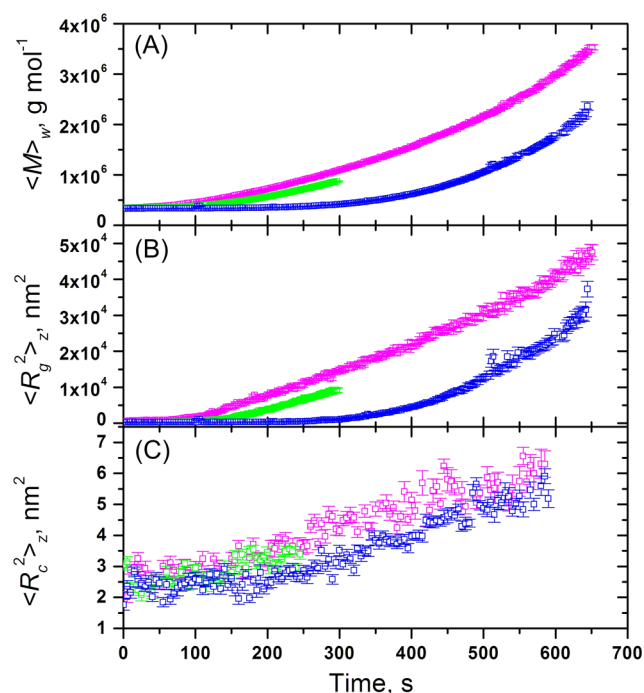


**Figure 2.** Typical time courses of  $\langle M \rangle_w$  (A),  $\langle R_g^2 \rangle_z$  (B), and  $\langle R_c^2 \rangle_z$  (C) from WA-MALS (A,B) and SAXS (C) data of FG polymerization induced by 0.05 NIH-unit Ancrod/mg FG. Magenta squares, FG 0.46 mg/mL in TBS; green squares, FG 0.59 mg/mL in TBS + CaCl<sub>2</sub> 1.25 mM; blue squares, FG 0.61 mg/mL in TBS + GPRP-NH<sub>2</sub> 0.02 mM (GPRP-NH<sub>2</sub>:FG molar ratio 10:1).

behaves differently, with  $\langle R_c^2 \rangle_z$  increasing somewhat faster as a function of  $\langle M \rangle_w$  than without GPRP-NH<sub>2</sub>.

**The Classic Polymerization Model Fails to Account for the Data.** In order to interpret the experimental data properly, extensive modeling was carried out, representing each FG unit with a cylinder of appropriate length and diameter, and beginning with the classic model of FG polymerization (see Materials and Methods, “Modeling”). In Figure 3, the results of a small subset of the simulations are compared with the experimental data. As already reported,<sup>21,22</sup> pure RLDS models with the ratio between the FpA release from a single FG molecule  $Q = 1$  up to  $Q = 16$  do not fit the  $\langle R_g^2 \rangle_z$  vs  $\langle M \rangle_w$  data at all (not shown). The very early phases can be fitted with a RLDS (or WLDS) model only with very high  $Q$  values (Figure 3A, dash-dot gray curve,  $Q = 90$ ), and the full curve can be approximated with a WLDS  $Q = 90$  model if a very low Kuhn length  $L_{k(DS)} = 280$  nm (meaning very flexible polymers) is used (Figure 3A, light gray curve). The effect of increasing  $Q$  is to skew the distributions toward longer polymers (see Supporting Information, Figure S8A). Polymer distributions calculated for  $Q = 90$  at various polymerization degrees leading to  $\langle M \rangle_w$  values comparable with the experimental data of Figure 3A are shown in Figure S8B. However, when we compare the  $\langle R_c^2 \rangle_z$  vs  $\langle M \rangle_w$  plots, it is evident that none of these models, all having the same cross-section distribution evolution, comes even close to matching the experimental data (Figure 3B, dash-dot light gray curve). This suggests that polymers thinner than those generated by the classic DS mechanism form in the initial stages of the reaction.

**An Alternative FG Polymerization Scheme.** We then made the assumption that the main polymerization mode involves only one center-to-end binding event between any two

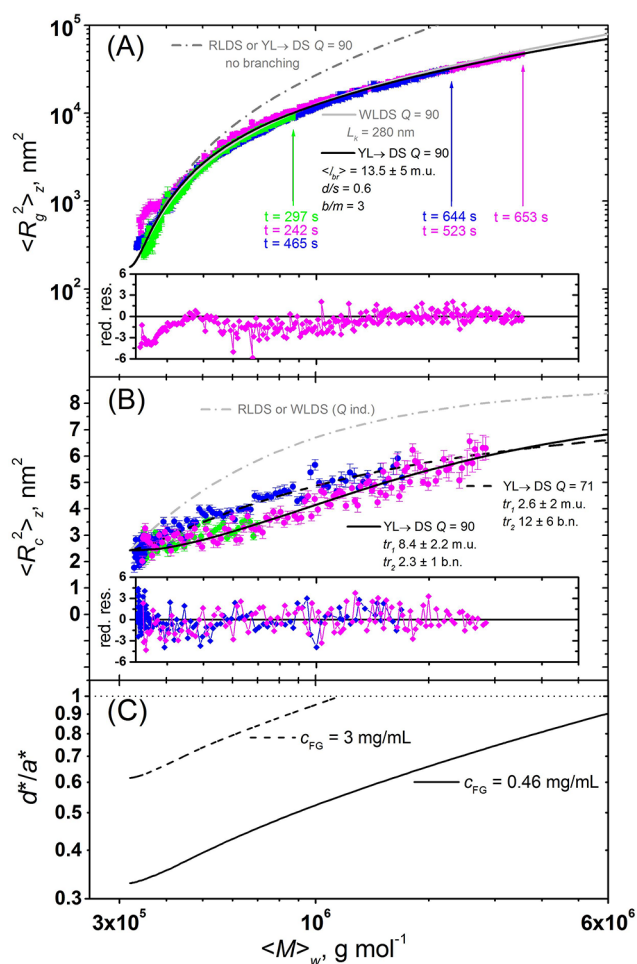


**Figure 3.** Coupled evolution of  $\langle R_g^2 \rangle_z$ ,  $\langle R_c^2 \rangle_z$  and  $\langle M \rangle_w$  and comparison with model curves. Double logarithmic plots of  $\langle R_g^2 \rangle_z$  vs  $\langle M \rangle_w$  (A, squares) and semilogarithmic plots of  $\langle R_c^2 \rangle_z$  vs  $\langle M \rangle_w$  (B, circles) for the three FG polymerization runs shown in Figure 2. Magenta symbols, TBS; green symbols, TBS + CaCl<sub>2</sub> 1.25 mM; blue symbols, TBS + GPRP-NH<sub>2</sub> 0.02 mM. In (A), the colored arrows indicate the reaction stopping times; in addition, below the green and blue arrows the corresponding reaction times for the other runs are reported. Both panels show superimposed several theoretical curves based on various models, with the corresponding parameters values (see text). In the insets, some reduced residuals [(fit - expt)/SD] are reported. (A) All with  $Q = 90$ : RLDS or YL→DS with no branching (dash-dot gray line); WLDS (light gray line); and YL→DS with branching (solid black line). The residuals are for the black line vs the magenta squares data. (B) RLDS or WLDS (dash-dot light gray line); YL→DS [branch parameters as in (A) with different  $Q$  and transition parameters; solid and dashed black lines]. The residuals are for the solid black and dashed black lines vs the magenta and blue circles data, respectively. (C) Calculated increase as a function of  $\langle M \rangle_w$  of the ratio  $d^*/a^*$  between the average diameters  $d^*$  of spheres having the same  $R_g$  as the fibrin monomer/polymers and their average distance  $a^*$ , for all the species generated in the YL→DS simulation best fitting the TBS experimental data (panel A, solid black line). Solid curve,  $c_{FG} = 0.5$  mg/mL; dashed curve,  $c_{FG} = 3$  mg/mL; the dotted line indicates the curves' theoretical limit (see text for details).

FG units, instead of the reciprocal double-binding called for by the half-staggered DS scheme. An example of a 15-mer of the resulting polymers, that we have dubbed “Y-ladder” (YL) because of their shape, is shown in Figure 4A, top, and their theoretical scattering properties were investigated (see Supporting Information, “YL models definition and scattering

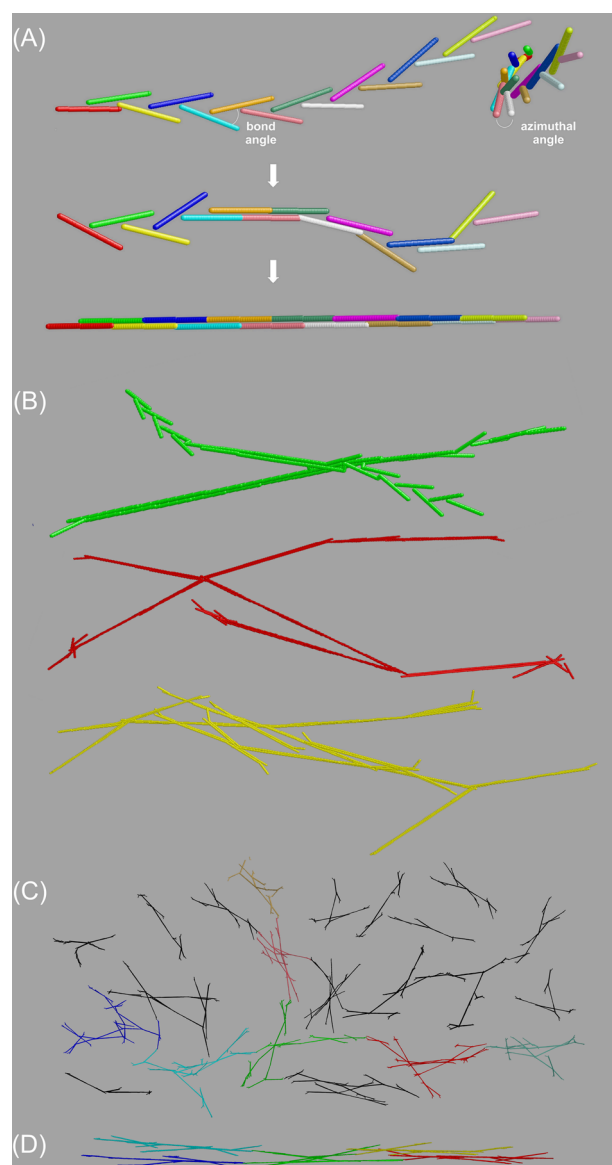


**Figure 4.** Models for fibrin polymers, based on the YL→DS hypothesis. (A) Top, two approximately perpendicular views of a “Y-ladder” (YL) fibril model generated with binding angles  $\theta = 30^\circ \pm 10^\circ$  and azimuthal angles  $\varphi = 5^\circ \pm 10^\circ$ ; middle, the YL→DS transition; bottom, a classic half-staggered, RLDS fibril. A different color is used for each fibrin monomer unit. (B) Models of developing highly branched fibrils (branching angles  $\theta_b = 20^\circ \pm 5^\circ$  and  $\varphi_b = 20^\circ \pm 20^\circ$ ; same color for all FG units) with  $\langle l_{br} \rangle = 13.5 \pm 5$  m.u.,  $d/s = 0.6$ ,  $b/m = 3$ ,  $tr_1 = 8 \pm 2$  m.u.,  $tr_2 = 2.4 \pm 1$  b.n. Top, a 50-unit fibril with a tetramolecular branch point; middle, a 175-unit fibril showing well-formed tri- and tetramolecular branch points and some incipient other branches; bottom, a 300-unit “lump” generated by repeated branching on a growing fibril (note the close proximity of most branches). (C) Artist's representation of how several “lumps” could interconnect in a structure that could either be a nucleus of the main final pervasive scaffold (colored lumps) or simply collapse on it, effectively increasing the fiber diameter (black lumps). (D) Artist's rendition showing how the collapsed branches from different lumps (colors) could generate thicker but low-density fibers.

properties” and Figure S6). This analysis revealed two important features: (a) DS and YL polymers of the same number of monomers have almost the same  $R_g^2$ , at least in the  $\langle M \rangle_w$  range of our data; and (b) in the  $q^2$  range in which we

analyze the SAXS data, very similar SAXS curves results for the YL polymers and the FG monomer (see Figure S6), leading to comparable  $R_c^2$  values. The fibril formation stage of the polymerization model was then completed by supposing that the second *A-a* binding event between any couple of FG monomers can be subsequently engaged along a growing YL polymer (YL→DS transition). An example of such an intermediate polymer is shown in Figure 4A, middle. In the end, a full DS fiber will be formed, as shown in Figure 4A, bottom. The DS fiber's twisted shape, obtained by random  $\varphi$  angles centered on small positive values, is consistent with EM data.<sup>37</sup> Calculated SAXS curves for YL→DS and full DS fibrils are also shown in Figure S6. Note that, from a reaction dynamics perspective, the initial single binding scheme presents two advantages: (1) it allows the binding of any unit with just one FpA released without chain termination effects, because the *a* holes are constitutively available on unbound FG molecules (instead, in the double-binding scheme a chain end cannot grow until the second FpA is cleaved); (2) given the random conformation of the *A* knob, it allows productive encounters between FG molecules with a greater range of diffusion-controlled relative orientations.

A further key feature of the YL→DS model is its potential for generating branching points by the occasional off-axis binding of fibrin monomers, giving rise to secondary growing chains as shown in Figure 4B. Importantly, the theoretical SAXS average profile of highly branched YL→DS 300-mers (Figure 4B, bottom) has a linear range and a slope very similar to that of the DS model (see Supporting Information, Figure S6), suggesting that this type of branching will not affect the measured fibrils' cross section. Equally important, the  $R_g^2$  of a branched polymer is significantly lower than that of a corresponding linear polymer for the same molecular weight, thus allowing a less steep increase of  $\langle R_g^2 \rangle_z$  vs  $\langle M \rangle_w$  as the reaction proceeds as compared to the pure RLDS, unbranched polymers. A detailed description of this complex modeling process can be found in the Supporting Information ("YL→DS models generation and parameters computation" and Figures S9–S11).

**The YL→DS with Branching Model Fits the Experimental Data.** Curves generated with YL polymers presenting both the YL→DS transition and branching can now be compared with the experimental  $\langle R_g^2 \rangle_z$  and  $\langle R_c^2 \rangle_z$  vs  $\langle M \rangle_w$  data. Although the Flory–Janmey bifunctional polycondensation scheme is formally not anymore appropriate to describe the YL→DS/branching mechanism, we have still employed it as a convenient means to generate different polymer distributions by varying *Q*. Simulations were then carried out by varying also the average length between branching points ( $\langle l_{br} \rangle$ ), the probability of having a double branch with respect to a single branch (*d/s*), the growth probability ratio between branches and the main chain (*b/m*), and the average distance from each growing end where the YL→DS transition starts taking place ( $tr_1$ ). Furthermore, since every end can also grow by addition of preformed oligomers, the YL→DS transition probability was enhanced as a function of the number of branches, by introducing a decay term ( $tr_2$ ) representing the average branch number (b.n.) above which the YL→DS transition occurs, independently of monomer position.

The results of our comprehensive polymerization model are quite startling. Although a very broad (though not exhaustive) search was performed involving the assessment of a large number of parameter combinations, we find that only a very

narrow subset could satisfy simultaneously the  $\langle R_g^2 \rangle_z$  vs  $\langle M \rangle_w$  and the  $\langle R_c^2 \rangle_z$  vs  $\langle M \rangle_w$  data. The best combination, optimized against the TBS data (magenta symbols), is reported in Figure 3 as the solid black lines. The computed residuals for the  $\langle R_g^2 \rangle_z$  vs  $\langle M \rangle_w$  data (Figure 3A, inset) show that, apart from the very early stages, where noise makes it difficult to evaluate the  $\langle R_g^2 \rangle_z$  values and the three conditions tested exhibit the greater differences, the rest of the process is quite well simulated with a surprisingly low  $\langle l_{br} \rangle = 13.5 \pm 5$  monomer units (m.u.), with *d/s* = 0.6 and *b/m* = 3. Distributions of the root-mean-square radii of gyration calculated according to these simulation parameters at four different  $\langle M \rangle_w$  values are shown in the Supporting Information (Figure S8C). The  $\langle R_c^2 \rangle_z$  vs  $\langle M \rangle_w$  data could be very well simulated, as shown by the solid black line and its associated residuals (Figure 3B and its inset), with these parameters and a YL→DS transition happening at  $tr_1 = 8.4 \pm 2.2$  m.u., decaying to zero when  $tr_2 = 2.3 \pm 1$  b.n. In practice, this means that when the polymers have more than about two branches, only new monomers added at the growing ends can still be in the YL configuration. We think that this reflects the addition of preformed polymers, already in the DS configuration. Importantly, the TBS + GPRP-NH<sub>2</sub>  $\langle R_g^2 \rangle_z$  and  $\langle R_c^2 \rangle_z$  vs  $\langle M \rangle_w$  data (Figure 3A,B, blue squares and circles) could best be reproduced with a practically identical  $\langle l_{br} \rangle = 14 \pm 5$  m.u., but *Q* was significantly smaller (*Q* = 71 vs *Q* = 90), and the YL→DS transition was much shortened to  $tr_1 = 2.6 \pm 2$  m.u. with the decay term increased to  $tr_2 = 12 \pm 6$  b.n. (thus becoming much less important). We interpret these changes as a consequence of the quite slower polymerization rate under these conditions (see Figure 2), producing less skewed polymer distributions and giving more time to the YL→DS transition to compete with elongation. It is also important to note that an *a posteriori* analysis with model curves suggests that the recovered  $\langle R_g^2 \rangle_z$  and  $\langle M \rangle_w$  data were not beyond the limit of our WAMALS capabilities. That is, if more-rigid, less-branched polymers were present, we would have been able to recover, up to a certain limit, the different  $\langle R_g^2 \rangle_z$  vs  $\langle M \rangle_w$  curves that they would have generated (see Supporting Information, "WAMALS data analysis" and Figure S5). While some underestimation of the experimental  $\langle R_g^2 \rangle_z$  values is still possible, especially at the longer reaction times, we are convinced that the recovered sets of parameters do reflect the basic properties of the FG polymerization mechanism.

## DISCUSSION

The physiological challenge faced by polymerizing fibrin is to form rapidly a pervasive 3D network and quickly make it strong and elastic enough so as to effectively trap and reinforce the initial platelet-rich plug. The modeling-based interpretation of our data reveals the elegant solution evolved since some kind of primitive system first formed ~500 million years ago.<sup>38,39</sup> At its very heart lies the basic bifunctionality of fibrinogen, with a pair of constitutively available sites (*a* holes). According to our proposed Y-ladder mode of polymerization, this allows any activated molecule to bind to either active or inactive units, be they other monomers or preformed polymers, without terminating effects even when just a single *A* knob is activated and free on a particular monomer. Highly skewed distributions toward longer polymers therefore arise, already helping to cover efficiently large distances. At the same time, the YL mechanism allows a much greater binding probability than the classic reciprocal double-binding and is intrinsically prone to generate a substantial number of branches along any growing fibril. A

large volume is then effectively swept, depleting it of monomers and smaller polymers. Eventually, some of the branches in different growing fibrils will make contact and produce bigger units, until a still rather nominally thin but pervasive scaffold is formed. An artist's rendering of this process can be seen in Figure 4C. A similar assumption for branching was made by Fogelson and Keener to explain the formation of nodal points in their FG polymerization simulation studies.<sup>40</sup> However, their model differs from ours in two basic aspects: their branching mechanism is planar, with full reciprocal binding between the units involved, and their "Z"-like polymers are transient structures with no further implications for elongation rates.

**The YL→DS with Branching Model Is Consistent with Microscopy Data.** It is interesting to compare our proposed mechanism of FG polymerization with the EM and time-resolved confocal microscopy work by Chernysh et al.,<sup>14</sup> although theirs was performed in different reaction conditions ( $c_{\text{FG}} = 1.5 \text{ mg/mL}$ , NaCl 150 mM, CaCl<sub>2</sub> 2.5 mM, thrombin 0.1 NIH-unit/mL). In the electron micrographs, they found a high proportion of long polymers during the lag time, consistent with our high  $Q$  values. However, no intermediate polymers above the tetramer level were found, perhaps because under their conditions such structures either are not stable or tend to produce larger aggregates. Instead, the evolving polymers visualized in the time-resolved confocal images bear a striking resemblance with the YL/branched structures generated in our simulations, which, we stress, were optimized only against the WA-MALS/SAXS data. Tri- and tetramolecular fibril branch points have been previously identified in EM work, but the latter were thought to occur at the lateral aggregation stage.<sup>41</sup>

**The YL→DS with Branching Model Can Account for Network Formation and Sudden Thickening of Low-Density Fibers.** To further verify whether our network formation model is consistent with the data, we have evaluated when the contact conditions between the growing fibrin polymers would be reached. To this end, we have calculated the ratio  $d^*/a^*$  between the average diameter  $d^*$  of virtual spheres with the same  $R_g$  as the polymers they represent and the average distance  $a^*$  between these spheres, for all polymers present in our simulation at any particular  $\langle M \rangle_w$  value (see Materials and Methods, "Contact Conditions Evaluation"). This ratio progressively increases until it reaches values close to 1 when spheres enter in contact, a hallmark of pervasive network formation.<sup>23,24,36</sup> The results of this simulation for the FG in TBS data ( $c_{\text{FG}} \approx 0.5 \text{ mg/mL}$ ) are shown as the solid line in Figure 3C. One can immediately see that, by the end of our experimental data ( $\langle M \rangle_w \approx 4 \times 10^6 \text{ g mol}^{-1}$ ), the collection of which was stopped just before the gel point,  $d^*/a^* \approx 0.8$ , meaning that at least the larger polymers are indeed already touching one another.<sup>36</sup> Of note is the observation that, at the network onset, more than 80% by weight of all FG molecules are still present in solution as monomers, as can be seen in Figure S8B.

The vast majority of the other branches, while still growing and further branching by the same mechanism, could then start to collapse on the arrested fibers, aided by the sideways cooperative interactions between fibrils (end of the "lag-time"). This fits quite nicely with our previous and recently reanalyzed LAELS data,<sup>23,24,42</sup> which demonstrate that, in the absence of Ca<sup>2+</sup>, at the end of the lag-time the pervasive scaffold is already formed, and only relatively minor rearrangements take place during the fiber lateral growth phase. On the other hand, the

data presently collected with added Ca<sup>2+</sup> until shortly before the end of the lag-time (see Figure 3A) indicate that, under these conditions, the thickening phase starts before the pervasive scaffold has formed. However, it should be considered that the early thickening we observe at  $c_{\text{FG}} \approx 0.5 \text{ mg/mL}$  in the presence of Ca<sup>2+</sup> is compensated, in true physiological conditions, by the higher  $c_{\text{FG}}$  in blood,  $\sim 3 \text{ mg/mL}$ , allowing an earlier onset of the network. This is nicely confirmed by the other calculation of  $d^*/a^*$  vs  $\langle M \rangle_w$  reported in Figure 3C (dashed line), where  $c_{\text{FG}}$  was set to 3 mg/mL and, based also on our previous results,<sup>21,22</sup> we assumed that the polymer distributions do not change significantly as a function of  $c_{\text{FG}}$ . As can be seen, the contact condition is now reached at  $\langle M \rangle_w \approx 1 \times 10^6 \text{ g mol}^{-1}$ , just about when the data collection in the presence of Ca<sup>2+</sup> was stopped (Figure 3A, green squares).

It is also worth mentioning that the collapse of connected branches leading to rapid fiber thickening can also account for the very low density of the fibrin fibers.<sup>23,42,43</sup> In fact, under our scheme a fully parallel arrangement of the fibrils is no longer required, and a fiber could be stabilized by a large number of interbranches' contact points. An artist's rendition of the branches' collapse process is shown in Figure 4D. Note that, due to the half-staggered geometry that governs the distribution of the branches' binding sites, the low-density fibers in our model will still produce, upon drying, the characteristic tight banding pattern with a  $\sim 23 \text{ nm}$  repeat observed in electron micrographs of fibrin fibers.<sup>44,45</sup>

#### Implications for the Fibers' Mechanical Properties.

The frequent branching scheme that we propose also has implications regarding fibrin elasticity. On stretching a fiber, the simplest elongation mechanism would involve the longitudinal slippage of DS fibrils within it. In our model, most fibrils within a fiber have at least a knob–hole anchorage point on another fibril, some of which under stress will eventually give way, allowing the slippage to take place. The elastic force is thus exerted mainly by the cooperative lateral interactions trying to maximize the contact points between the collapsed DS fibrils in the low-density fibers. However, new knob–hole anchorage points might re-form on another location either pre-existing or freed by the slippage of another fibril. This would explain why many non-cross-linked fibers do not return to their original length but buckle once tension is released.<sup>46</sup> Cross-linking is the formation of covalent isopeptide bonds between specific Gln/Lys residues in the C-terminals ends of the  $\gamma$  chains and in the  $\alpha$ C domains.<sup>6,7</sup> Importantly, the predominant interfibrils' cross-linking between the  $\alpha$ C domains physiologically takes place later in fibrin formation, when the initially very elastic network that had time to adapt to the local stresses needs strengthening to avoid breakage.

## CONCLUSIONS

In conclusion, the simultaneous measurement of the FG polymerization progress ( $\langle M \rangle_w$ ) and of the polymer size ( $\langle R_g^2 \rangle_z$ ) and thickness ( $\langle R_c^2 \rangle_z$ ) made possible by our rapid-mixing WA-MALS/SAXS setup has led us to propose a revised mechanism for fibrin polymerization that can explain a wealth of experimental observations. Implicit (e.g., ref 40) or explicit (e.g., ref 47) kinetic computer simulations should be possible to test further and refine the proposed mechanism. We point out that although the snake venom enzyme Ancrod was used to avoid complicating the interpretation by even limited FpB release, the present data are quite similar to those we previously collected using thrombin and only a WA-MALS with a more

limited angular range.<sup>21,22</sup> Further work with recombinant FG species with missing<sup>48</sup> or human/chicken hybrid<sup>49</sup>  $\alpha$ C regions, and with either uncleavable FpB's or nonbinding B knobs/unavailable b holes and thrombin as the enzyme, is planned. It should help to clarify the role played by the largely unstructured A $\alpha$  chain appendages, which are also functionally important for FG adhesion,<sup>50,51</sup> and refine the model parameters under closer to physiological conditions.

## ■ ASSOCIATED CONTENT

### ● Supporting Information

Figures S1–S11; details of sample preparation, stopped-flow/WA-MALS/SAXS setup, WA-MALS data analysis, SAXS data analysis, YL→DS models generation, and parameters computation; results of YL models definition and scattering properties. This material is available free of charge via the Internet at <http://pubs.acs.org>.

## ■ AUTHOR INFORMATION

### Corresponding Author

[mattia.rocco@hsanmartino.it](mailto:mattia.rocco@hsanmartino.it)

### Present Addresses

<sup>∇</sup>Jülich Centre for Neutron Science, Outstation at MLZ, D 85747 Garching, Germany

<sup>¶</sup>Sviluppo Terapie Innovative, IRCCS AOU San Martino-IST, I 16132 Genova, Italy

### Author Contributions

<sup>○</sup>M.R., M.M., P.V., F.F., and J.P. contributed equally.

### Notes

The authors declare no competing financial interest.

## ■ ACKNOWLEDGMENTS

We thank Ms. A. Aprile (IRCCS AOU San Martino-IST) for excellent technical assistance, P. Roblin (INRA and SWING beamline, Synchrotron SOLEIL) for help with the measurements, D. Friscione (Alfatech, Genova, Italy) for logistic support, C. Mérigoux (IBBMC, Orsay, France) for help with Figure S7, C. Rosano (IRCCS AOU San Martino-IST) for atomic-scale FG models, E. Brookes (UTHSCSA, San Antonio, TX, USA) for timely improvements to the US-SOMO program, and S. T. Lord (University of North Carolina, Chapel Hill, NC, USA) for discussions. We are indebted to T. Azoulay (Wyatt Technology France) for providing crucial equipment. The research leading to these results has received funding from the European Community's Seventh Framework Programme (FP7/2007-2013) under BioStruct-X (grant agreement No. 283570; award no. 428/2012 to M.R.).

## ■ REFERENCES

- (1) Doolittle, R. F. The molecular biology of fibrin. In *The Molecular Basis of Blood Diseases*, 3rd ed.; Stamatoyannopoulos, G., Majerus, P. W., Perlmutter, R. M., Varmus, H., Eds.; Saunders: Philadelphia, 2000; pp 719–739.
- (2) Blombäck, B. *Thromb. Res.* **1996**, *83*, 1–75.
- (3) Boccaccio, C.; Medico, E. *Cell. Mol. Life Sci.* **2006**, *63*, 1024–1027.
- (4) Spotnitz, W. D. *World J. Surg.* **2010**, *34*, 632–634.
- (5) Eylich, D.; Göpferich, A.; Blunk, T. *Adv. Exp. Med. Biol.* **2006**, *585*, 379–392.
- (6) Doolittle, R. F. *Annu. Rev. Biochem.* **1984**, *53*, 195–229.
- (7) Weisel, J. W. *Adv. Protein Chem.* **2005**, *70*, 247–299.
- (8) Spraggon, G.; Everse, S. J.; Doolittle, R. F. *Nature* **1997**, *389*, 455–462.

- (9) Yang, Z.; Kollman, J. M.; Pandi, L.; Doolittle, R. F. *Biochemistry* **2001**, *40*, 12515–12523.
- (10) Kollman, J. M.; Pandi, L.; Sawaya, M. R.; Riley, M.; Doolittle, R. F. *Biochemistry* **2009**, *48*, 3877–3886.
- (11) Yang, Z.; Mochalkin, I.; Doolittle, R. F. *Proc. Natl. Acad. Sci. U.S.A.* **2000**, *97*, 14156–14161.
- (12) Fowler, W. E.; Hantgan, R. R.; Hermans, J.; Erickson, H. P. *Proc. Natl. Acad. Sci. U.S.A.* **1981**, *78*, 4872–4876.
- (13) Medved, L.; Ugarova, T.; Veklich, Y.; Lukinova, N.; Weisel, J. J. *Mol. Biol.* **1990**, *216*, 503–509.
- (14) Chernysh, I. N.; Nagaswami, C.; Weisel, J. W. *Blood* **2011**, *117*, 4609–4614.
- (15) Hategan, A.; Gersh, K. C.; Safer, D.; Weisel, J. W. *Blood* **2013**, *121*, 1455–1458.
- (16) Müller, M.; Burchard, W. *Biochim. Biophys. Acta* **1978**, *537*, 208–225.
- (17) Hantgan, R. R.; Hermans, J. *J. Biol. Chem.* **1979**, *254*, 11272–11281.
- (18) Wiltzius, P.; Dietler, G.; Känzig, W.; Hofmann, V.; Häberli, A.; Straub, P. W. *Biophys. J.* **1982**, *38*, 123–132.
- (19) Wiltzius, P.; Dietler, G.; Känzig, W.; Häberli, A.; Straub, P. W. *Biopolymers* **1982**, *21*, 2205–2223.
- (20) Kubota, K.; Kogure, H.; Masuda, Y.; Toyama, Y.; Kita, R.; Takahashi, A.; Kaibara, M. *Colloid Surf. B: Biointerfaces* **2004**, *38*, 103–109.
- (21) Bernocco, S.; Ferri, F.; Profumo, A.; Cuniberti, C.; Rocco, M. *Biophys. J.* **2000**, *79*, 561–583.
- (22) Rocco, M.; Bernocco, S.; Turci, M.; Profumo, A.; Cuniberti, C.; Ferri, F. *Ann. N.Y. Acad. Sci.* **2001**, *936*, 167–185.
- (23) Ferri, F.; Greco, M.; Arcòvito, G.; Bassi, F. A.; De Spirito, M.; Paganini, E.; Rocco, M. *Phys. Rev. E* **2001**, *63*, 031401-1–031401-17.
- (24) Ferri, F.; Greco, M.; Arcòvito, G.; De Spirito, M.; Rocco, M. *Phys. Rev. E* **2002**, *66*, 011913-1–011913-13.
- (25) Janmey, P. A. *Biopolymers* **1982**, *21*, 2253–2264.
- (26) Ferri, F.; Greco, M.; Rocco, M. *Macromol. Symp.* **2000**, *162*, 23–44.
- (27) Glatter, O.; Kratky, O. *Small-Angle X-ray Scattering*; Academic Press: Waltham, MA, 1982.
- (28) Bell, W. R., Jr. *Drugs* **1997**, *54*, 18–30.
- (29) Cardinali, B.; Profumo, A.; Aprile, A.; Byron, O.; Morris, G.; Harding, S. E.; Stafford, W. F.; Rocco, M. *Arch. Biochem. Biophys.* **2010**, *493*, 157–168.
- (30) David, G.; Pérez, J. J. *Appl. Crystallogr.* **2009**, *42*, 892–900.
- (31) Preux, O.; Durand, D.; Huet, A.; Conway, J. F.; Bertin, A.; Boulogne, C.; Drouin-Wahbi, J.; Trévarin, D.; Pérez, J.; Vachette, P.; Boulanger, P. *J. Mol. Biol.* **2013**, *425*, 1999–2014.
- (32) Brookes, E.; Pérez, J.; Cardinali, B.; Profumo, A.; Vachette, P.; Rocco, M. *J. Appl. Crystallogr.* **2013**, *46*, 1823–1833.
- (33) Hjelm, R. P., Jr. *J. Appl. Crystallogr.* **1985**, *18*, 452–460.
- (34) Raynal, B.; Cardinali, B.; Grimbergen, J.; Profumo, A.; Lord, S. T.; England, P.; Rocco, M. *Thromb. Res.* **2013**, *132*, e48–e53.
- (35) Spotorno, B.; Piccinini, L.; Tassara, G.; Ruggiero, C.; Nardini, M.; Molina, F.; Rocco, M. *Eur. Biophys. J.* **1997**, *25*, 373–384; **1997**, *26*, 417 (erratum).
- (36) De Gennes, P. G. *Scaling concepts in polymer physics*; Cornell University Press: Ithaca, NY, 1979; Chapter 3.
- (37) Weisel, J. W.; Nagaswami, C.; Makowski, L. *Proc. Natl. Acad. Sci. U.S.A.* **1987**, *84*, 8991–8995.
- (38) Doolittle, R. F. *Cold Spring Harbor Symp. Quant. Biol.* **2009**, *74*, 35–40.
- (39) Patthy, L. *Blood Coagul. Fibrinol.* **1990**, *1*, 153–166.
- (40) Fogelson, A. L.; Keener, J. P. *Phys. Rev. E* **2010**, *81*, 051922-1–051922-9.
- (41) Mosesson, M. W.; DiOrto, J. P.; Siebenlist, K. R.; Wall, J. S.; Hainfeld, J. F. *Blood* **1993**, *82*, 1517–1521.
- (42) Magatti, D.; Molteni, M.; Cardinali, B.; Rocco, M.; Ferri, F. *Biophys. J.* **2013**, *104*, 1151–1159.
- (43) Carr, M. E., Jr.; Hermans, J. *Macromolecules* **1978**, *11*, 46–50.
- (44) Hall, C. E. *J. Biol. Chem.* **1949**, *179*, 857–864.

- (45) Stryer, L.; Cohen, C.; Langridge, R. *Nature* **1963**, *197*, 793–794.
- (46) Münster, S.; Jawerth, L. M.; Leslie, B. A.; Weitz, J. I.; Fabry, B.; Weitz, D. A. *Proc. Natl. Acad. Sci. U.S.A.* **2013**, *110*, 12197–12202.
- (47) Lattuada, M.; Wu, H.; Sandkuhler, P.; Sefcik, J.; Morbidelli, M. *Chem. Eng. Sci.* **2004**, *59*, 1783–1798.
- (48) Gorkun, O. V.; Henschen-Edman, A. H.; Ping, L. F.; Lord, S. T. *Biochemistry* **1998**, *37*, 15434–15441.
- (49) Ping, L.; Huang, L.; Cardinali, B.; Profumo, A.; Gorkun, O. V.; Lord, S. T. *Biochemistry* **2011**, *50*, 9066–9075.
- (50) Jung, S. Y.; Lim, S. M.; Albertorio, F.; Kim, G.; Gurau, M. C.; Yang, R. D.; Holden, M. A.; Cremer, P. S. *J. Am. Chem. Soc.* **2003**, *125*, 12782–12786.
- (51) Belkin, A. M.; Tsurupa, G.; Zemskov, E.; Veklich, Y.; Weisel, J. W.; Medved, L. *Blood* **2005**, *105*, 3561–3568.